CHEMICAL SCIENCE

Structural reorganization of CuO/Cu$_2$[Fe(CN)$_6$] nanocomposite: characterization and electrocatalytic effect for the hydrogen peroxide reduction

WALLONILSON V. RODRIGUES, STEFFANE Q. NASCIMENTO, WESLEY Y.S. SILVA,
SANOELLE F. L. QUINZEIRO, ROBERTO A.S. LUZ & WELTER CANTANHÊDE

Abstract: We report the study on the formation of the Cu$_2$[Fe(CN)$_6$] nanocomposite, which was obtained from copper oxide nanoparticles (CuO NPs) and Prussian Blue precursors. UV-vis analysis indicated that Cu$_{2+}$ ions are released from CuO NPs, while Fe$_{3+}$ ions are adsorbed onto the structure of CuO due to a sharp increase in zeta potential (from -30 to 0 mV) after the formation of the Cu$_2$[Fe(CN)$_6$]. Moreover, energy dispersive spectroscopy confirmed that Fe$_{3+}$ ions are trapped in the CuO NPs structure. The CuO/Cu$_2$[Fe(CN)$_6$] nanocomposite exhibited the monoclinic and face-centered cubic phases that correspond to the CuO and Cu$_2$[Fe(CN)$_6$] components. Cyclic voltammetry (CV) for the Nanocomposite modified electrode revealed two well-defined redox couples at -0.073 (($E_{1/2}$)$_1$) and 0.665 mV (($E_{1/2}$)$_2$), attributed to the conversion of Cu$_{2+}$ to Cu$_+$ and CuFe$_{2+}$ CuFe$_{3+}$ pairs, respectively, which is similar to those in the CuO and Cu$_2$[Fe(CN)$_6$] components. Furthermore, the catalytic activity of the nanocomposite towards hydrogen was investigated through CV, where the reduction of H$_2$O$_2$ led to increased currents for the electrochemical process associated with the first redox pair. In contrast, for isolated materials (CuO NPs and Cu$_2$[Fe(CN)$_6$]), there was no significant increase in the current associated with either redox pair.

Key words: nanocomposite, prussian blue analogue, supramolecular properties, hydrogen peroxide.

INTRODUCTION

Nanocomposites can be defined as multiphase solid materials in which at least one of the phases is present in the nanometer range (Jelinkova et al. 2019, Rawtani et al. 2019). The use of nanocomposites can impart structural properties and performance capabilities that are significantly different from those of the original components. Several nanomaterials such as magnetite (Santos et al. 2016), graphene (Fattahi et al. 2019), metallic nanoparticles (Lopes et al. 2018), inorganic complexes (Silva et al. 2013), and biological nanoparticles (Roy et al. 2020) have been used as components for complex structure design on the basis of a combination of the building blocks. Using this approach, magnetic (Ayubi et al. 2019), electrical (Alfaify & Shkyr 2019), optical (Soliman & Vshivkov 2019), adsorptive (Singh et al. 2016), catalytic (Alimard 2019), and antibacterial (Dadi et al. 2019) properties can be improved at the nanoscale.

The main materials used for the preparation of nanocomposites include Prussian Blue (PB) and Prussian Blue analog (PBA) complexes. These compounds are often studied by the scientific community because of their structural, electrochemical, and thermal properties (Xu et

al. 2017) as well as their simple preparation and low cost. PB and PBA are complexes with the $M_a^{x+}[M_b(CN)_6]_y.nH_2O$ structural formula, where for PB, $M_a = M_b = Fe$ (Zakaria & Chikyou 2017) and for PBA, M_a and M_b = a transition element such as Cu, Mn, Co, Ni or Fe (Bie et al. 2018). In particular, the most promising PBA compounds include copper hexacyanoferrate nanoparticles, which impart high adsorption capacity (Tao et al. 2019), and undergo electrochemical processes in different media (Baioni et al. 2008). These compounds have the formula $M_xCu_y[Fe(CN)_6].nH_2O$, where copper is usually present in the divalent cationic form, while iron is present in both oxidation states, (II) and (III). In addition to these species, the structure may contain alkali metal cations (M^+) and hydrating water molecules.

PB and its derivatives are widely used in electrochemical studies, mainly because of the stability and characteristic redox reactions of the $[M^{2+}-CN-Fe^{3+}]$ fragment, which is able to mediate and catalyze electrochemical reactions of peroxide (Chu et al. 2017). However, the use of PB in redox processes is limited mainly to the use of electrolytes with a small hydrodynamic radius (up to 0.1 nm), which are capable of occupying the interstices of its structure, ensuring electroneutrality and enabling electron transfer (Ricci 2005). On the other hand, a PBA complex has been reported to demonstrate electrochemical activity in a variety of electrolytes (Asai et al. 2018).

Additionally, PB and PBA compounds have been used to develop new nanocomposites for various applications (Li et al. 2019). For example, Fu et al. (2014) investigated the use of an $Fe_3O_4@$PB nanocomposite in the treatment of cancer cells. Xu et al. (2015) developed electrochemical glucose quantification sensors based on a PB system decorated with silver nanoparticles. In catalyzed reactions, Li et al. (2015) analyzed peroxide catalysis with PB covering graphene

structures. In a study related to environment preservation, Ai et al. (2019) followed the degradation of Rhodamine B organic dyes by a PBA $Co_3[Fe(CN)_6]_2$ nanocomposite on a zeolitic support. It is interesting to note that $Cu_2[Fe(CN)_6]$ has been used in research involving supercapacitors (Song et al. 2019), electronic peroxide sensors (Ventura et al. 2018), and biosensors (Mazeikiene et al. 2018) and studies on decontamination of heavy metals (Pshinko et al. 2018). The use of this PBA, which is monitored by means of electroanalytical techniques such as cyclic voltammetry (CV), is based on the $CuFe^{2+}/CuFe^{3+}$ redox process. It is noteworthy that in most cases, iron is the only electroactive species in the compound.

Copper oxide nanoparticles (CuO NPs) belong to the p-type semiconductor oxide class with a band gap of 1.2–2.0 eV (Sreeju et al. 2018). They are known for their low solubility, high porosity, and thermal stability; owing to these properties, CuO NPs are used in the degradation of organic dyes (Quirino et al. 2018) and as supercapacitors and bactericidal agents (Vasantharaj et al. 2018).

Electrochemical sensors are currently being used for the determination of analytes such as glucose (Ding et al. 2019), H_2S (Brown et al. 2018), dopamine (Wang et al. 2019), hydrogen peroxide (Bach et al. 2019), and cholesterol (Thakur et al. 2019). The use of CuO NPs facilitates the involvement of cationic species (Cu^+, Cu^{2+}, and Cu^{3+}) in applications close to 0 V in neutral, acidic, and basic media (Vázquez et al. 2019, Foroughi et al. 2018). Equations (1)–(3) represent the formation of some of these species:

$$Cu^{2+} \longrightarrow Cu^{3+} + e^- \ (1)$$

$$Cu^{2+} + e^- \longrightarrow Cu^+ \ (2)$$

$$Cu^+ + e^- \longrightarrow Cu^0 \ (3)$$

Hydrogen peroxide (H_2O_2) is one of the most important compounds in the chemical industry (Teodoro et al. 2019). Moreover, high levels of H_2O_2 in biological tissues may indicate a state of oxidative stress, an infection, or presence of cancer cells (Nerush et al. 2019). In this context, devices that measure the concentration of H_2O_2 in various media are of utmost importance. We report below a novel $CuO/Cu_2[Fe(CN)_6]$ nanocomposite that takes advantage of the assembly process of $Cu_2[Fe(CN)_6]$ and CuO NPs. The formation, structural organization, electronic properties, and electrochemical performance of the nanocomposite are investigated using zeta-potential data, ultraviolet–visible (UV–vis) and Fourier-transform infrared (FTIR) spectroscopy, X-ray diffraction (XRD), transmission electron microscopy (TEM), scanning electronic microscopy (SEM), energy dispersive spectroscopy (EDS), and CV measurements.

MATERIALS AND METHODS

Chemicals and materials

All reagents were of analytical grade and were used without further purification. In the synthesis of PB, potassium hexacyanoferrate(II) trihydrate PA ($K_4[Fe(CN)_6].3H_2O$, Isofarma), iron (III) chloride hexahydrate 99% ($FeCl_3.6H_2O$, Sigma Aldrich), and citric acid PA ($C_6H_8O_7$, Dinâmica) were used. Copper (II) sulfate pentahydrate PA ($CuSO_4.5H_2O$) and sodium hydroxide 99% (NaOH), purchased from Dinâmica and Sigma-Aldrich, respectively, were used to prepare copper oxide nanoparticles. These reagents were used to

synthesize the $Cu_2[Fe(CN)_6]$ complex and the physical mixture containing CuO and PB. The acetate buffer was prepared by titrating acetic acid (CH_3COOH, Dinâmica) into a potassium hydroxide [3] 85% solution (KOH, Sigma-Aldrich). Hydrogen peroxide (H_2O_2, 3%) was purchased from Rioquímica. The water used in the experiments was purified by the Purelab Option-Q (Elga) system with a resistance equal to 18.2 MΩ cm.

Synthesis of CuO nanoparticles

The CuO NPs were prepared using the synthetic strategy described by Kamila & Venugopal (2017), with minor changes. In this procedure, 20 mL of 0.1 mol L^{-1} $CuSO_4.5H_2O$ solution (2.0×10^{-3} mol) was prepared and added slowly to a reaction flask containing 20 mL of 0.2 mol L^{-1} NaOH solution (4.0×10^{-3} mol). The product was centrifuged three times for 5 min at 3500 rpm, dried in an oven at 60°C for 2 h, and calcined at 400°C for 4 h.

Synthesis of $Cu_2[Fe(CN)_6]$ complex

The $Cu_2[Fe(CN)_6]$ complex was prepared using a 2:1 mol ratio between the precursors $CuSO_4.5H_2O$ and $K_4[Fe(CN)_6]$, as described by Kim et al. (2017). A solution of $K_4[Fe(CN)_6].3H_2O$ (0.0845 g, 2.0×10^{-4} mol, in 40 mL of water: 5.0×10^{-3} mol L^{-1}) was added slowly to a solution of $CuSO_4.5H_2O$ (0.100 g, 4.0×10^{-4} mol, in 40 mL of water: 1.0×10^{-2} mol L^{-1}) in a current of nitrogen at 25°C. The reddish precipitate was separated by centrifuging three times for 5 min at 3500 rpm in solution (50% v/v ethanol/water) and the powder was dried at 60°C for 2 h.

Synthesis of $CuO/Cu_2[Fe(CN)_6]$ nanocomposite

The $CuO/Cu_2[Fe(CN)]_6$ nanocomposite was prepared using the synthetic strategy described by Carvalho et al. (2018). The CuO NPs powder (0.100 g, 1.26×10^{-3} mol) was added to an aqueous solution of $FeCl_3.6H_2O$ (0.108 g, 4.0×10^{-3} mol, in

40 mL of water: 0.100 mol L^{-1}). This was followed by the slow dropwise addition of 40 mL of 0.100 mol L^{-1} $K_4[Fe(CN)_6]$ (0.169 g, 4.0 × 10^{-4} mol) to the reaction mixture, which was sonicated for 1 min and heated in a water bath to 60°C under nitrogen. Finally, the brownish-red CuO/$Cu_2[Fe(CN)_6]$ product was centrifuged three times (solution 50% v/v ethanol/water) in order to remove the non-adsorbed or weakly adsorbed CuO and Fe^{3+} species on the nanocomposite surface, and dried at 60°C for 2 h.

Characterization

UV–vis spectra of solutions and dispersions of the precursors and reaction products were recorded with an Agilent Technologies Cary 60 UV-Vis spectrophotometer using a quartz cuvette with 1 cm optical path, in the wavelength range 200 to 900 nm. Infrared spectra between 400 and 4000 cm^{-1} were obtained with a PerkinElmer Spectrum 100 FTIR spectrometer, using pellets composed of 99 mg of KBr and 1 mg of the sample material. The spectra were normalized with maximum and minimum values corresponding to 1.0 and 0.0, respectively. Zeta potentials were used to verify the charges on the nanoparticle surfaces. For these investigations, CuO NPs, $Cu_2[Fe(CN)_6]$, and nanocomposite dispersions of 2.0 ×10^{-2} g L^{-1} of each component were prepared. Separately, a 1 mL aliquot of the heated dispersion containing CuO NPs and Fe^{3+} ions, from the synthesis step described in experimental section, was diluted to a concentration of 2.0 ×10^{-2} g L^{-1} CuO. Analyses were performed using Horiba SZ-100 nano-sizer equipment. TEM images were used to investigate the morphology and particle size distribution of the nanoparticles, using a JEOL JEM 2100 microscope (LAB6 filament), with an accelerating voltage of 200 kV. The TEM images were obtained digitally by use of the Image–Pro Plus software package. The crystallinity and polymorphic forms were analyzed by XRD on a Panalytical Empyrean diffractometer with a CoK radiation source, using a 2θ scanning range from 10° to 70°. Finally, the precursor (CuO/Fe^{3+}) was characterized using a Field Emission Scanning Electron Microscope (FESEM) (QUANTA 250 FEI, FEI Company, Eindhoven, The Netherlands), coupled with elemental analysis by EDS (EDAX Apollo X, FEI Company, Eindhoven, The Netherlands). The CV procedures were performed with the potentiostat/galvanostat Autolab PGSTAT128N equipment, coupled to a 3 mL electrolytic cell comprising a 3 mm diameter glassy carbon electrode, a 0.35 cm^2 area platinum counter electrode, and a saturated calomel electrode (SCE) as reference. An acetic acid/acetate buffer with pH 4.1 was used as a support electrolyte, and N_2 gas was bubbled for ten minutes before the analysis. The potential window employed was -0.6 to 1.2 V. To obtain cast films, dispersions (6 mg mL^{-1}) of CuO and $Cu_2[Fe(CN)_6]$ were prepared, and 10 µL of each solution was transferred by the *drop coating* method to the glassy carbon electrode (GCE). The voltammetry experiment on the nanocomposite was performed after collecting 20 µL of the dispersion and drying the cast films at 40°C for approximately 20 min.

Catalytic activity of CuO, $Cu_2[Fe(CN)_6]$, and CuO/$Cu_2[Fe(CN)_6]$ modified electrodes

The electrocatalytic activity of carbon-modified electrodes of CuO, $Cu_2[Fe(CN)_6]$, and CuO/$Cu_2[Fe(CN)_6]$ was investigated by CV upon addition of hydrogen peroxide at concentrations ranging from 3.0 × 10^{-4} to 3.0 × 10^{-3} mol L^{-1}, with an acetate buffer of pH 4.1. We used a scan rate of 25 mV s^{-1} at room temperature (25°C).

RESULTS AND DISCUSSION

Unexpected formation of CuO/Cu$_2$[Fe(CN)$_6$] nanocomposite

Initially, our intention was to synthesize a CuO/Fe$_4$[Fe(CN)$_6$]$_3$ nanocomposite. Our strategy for this was accomplished in two different ways: 1) After mixing the CuO and Fe^{3+} species, the [Fe(CN)$_6$]$^{4-}$ species was added; and 2) the [Fe(CN)$_6$]$^{4-}$ ion complex was added to a mixture containing CuO, Fe^{3+} species, and citric acid. For both systems, the syntheses were performed with heating (at 60°C). In contrast to what has been observed for other nanocomposites, such as PB/β-cyclodextrin (Cantanhêde et al. 2015), PB/Fe$_2$O$_3$ (Santos et al. 2014), and PB/AuNPs/TiO$_2$ NPs (Gao et al. 2014), the PB species containing the [Fe^{II}-CN-Fe^{III}] fragment was not formed. According to Cantanhêde et al. (2015), the mechanism for PB/cyclodextrin polymer nanocomposite formation occurs in two steps. First, the Fe^{2+} species binds to the OH$^-$ sites of the polymer chain, and after this, the Fe^{2+} species coordinates to the cyanide ligand of the [Fe^{III}(CN)$_6$]$^{3-}$ ion. To explain the formation of the nanocomposite, we conducted a preliminary study. Before adding the [Fe(CN)$_6$]$^{4-}$ species, the zeta potential for the isolated CuO NPs was measured to be -30 mV. However, after the addition of the Fe^{3+} species to the mixture, the measured zeta potential increased to 0, suggesting that the Fe^{3+} ions were adsorbed on the surface of the CuO NPs. The UV-Vis spectrum of the mixture containing CuO NPs and Fe^{3+} ions (Figure S1- Supplementary Material) exhibited a broad band at 800 nm (e = 14 L mol cm^{-1}), which was assigned to the d-d transitions characteristic of [Cu(H$_2$O)$_6$]$^{2+}$ in the supernatant. It is interesting that the band at 295 nm, characteristic of [Fe(H$_2$O)$_6$]$^{3+}$ was not observed. These observations suggest that strong adsorption of ferric ions occurs on the surface of CuO NPs, with the release of Cu^{2+} ions from the crystalline structure (into the mixture), which then react with [Fe(CN)$_6$]$^{4-}$ to form Cu$_2$[Fe(CN)$_6$]. In another test, potassium thiocyanate (KSCN) was added to a dispersion containing CuO and Fe^{3+} species, and heated (at 60°C), in order to investigate the possibility of obtaining the [Fe(SCN)]$^{2+}$ complex (K_f = 2.0 × 10^6). In aqueous solution, this complex is red in color and exhibits a characteristic absorption band at 460 nm in the UV-Vis spectrum (Figure S1b). When drops of a 0.1 mol L^{-1} solution of KSCN were added, a greenish-colored complex was formed, which exhibited an absorption band at 338 nm, characteristic of the Cu(SCN)$^+$ ion (K_f = 5.6 × 10^3). With this experiment, we have clearly demonstrated the inability of Fe^{3+} ions to react with [Fe(CN)$_6$]$^{4-}$, owing to their attraction toward CuO NPs. Surprisingly, the Cu^{2+} ions released by CuO NPs are able to react in solution with ferrocyanide ions, producing the complex Cu$_2$[Fe(CN)$_6$].

To reinforce the justification, the elemental composition and morphology resulting from this interaction (CuO + Fe^{3+}) of the solid phase were recorded by SEM (Figure S2) and EDS (Figure S3). The SEM analysis indicates (Figure S2) the formation of polydisperse particles having cubic shapes. As expected, large amounts of Cu and O from the CuO NPs, and a significant iron fraction as well as some impurities, were observed, as shown in (Table SI- Supplementary Material). The results show that the copper atoms (14.6%) are in the same molar ratio with the iron atoms (16.9%) in the solid phase. The effect of the strong interaction between the CuO NPs and Fe^{3+} ions can be rationalized according to Pearson's acid-base theory (Pearson 1963). According to the theory, the O^{2-} anion (which is a hard base) has a greater tendency to bind with hard acids (which are typically highly charged cations with low polarizing power). Analyzing the nature of the Fe^{3+} and Cu^{2+} ions, these cations are classified

as hard and borderline acids, respectively. Thus, it is possible to release copper ions in exchange for iron atoms in the crystalline structure of CuO, with the adsorption of Fe^{3+} ions, based on a Pearson acid-base reaction (Pearson 1963). Similarly, the ionic radii of the Cu^{2+} and Fe^{3+} species are 73 and 64 pm, respectively, with a radius ratio of 1.14 for Cu^{2+}/Fe^{3+}; this is very close to unity, a value that would also facilitate confinement of the ferric ions in the CuO unit cell. Finally, the zeta potentials for the $Cu_2[Fe(CN)_6]$ complex and the nanocomposite were -29 mV and +28 mV, respectively, indicating that this structure has stoichiometric defects due to the reaction conditions. It is important to note that the synthesis of the $CuO/Cu_2[Fe(CN)_6]$ nanocomposite was carefully investigated to confirm its reproducibility.

Spectroscopic studies for the formation of $CuO/Cu_2[Fe(CN)_6]$ nanocomposite

In order to investigate the unexpected formation of the $CuO/Cu_2[Fe(CN)_6]$ nanocomposite, we carried out the following spectroscopic studies. The relative absorbance spectra for both the precursor compounds, as well as the nanocomposite, are shown in Figure 1. The inset shows the Tyndall effect exhibited by the nanocomposite. This phenomenon is observed as a result of light scattering in dispersions containing particles of colloidal dimensions (1–100 nm), and its occurrence, thus, confirms the colloidal nature of this material. UV-Vis spectra for the $Cu_2[Fe(CN)_6]$ complex (Figure 1, curve b) and nanocomposite (Figure 1, curve c) exhibited a band with λ_{max} at 479 nm, which is attributed to metal-to-ligand charge-transfer (MLCT) (Moulik et al. 1999, Kong et al. 2005). The CuO NPs (Figure 1, curve a) exhibited a characteristic absorption band with $\lambda_{max} \sim 243$ nm (Ghorbani et al. 2018, Kumar et al. 2019), which has been attributed to a
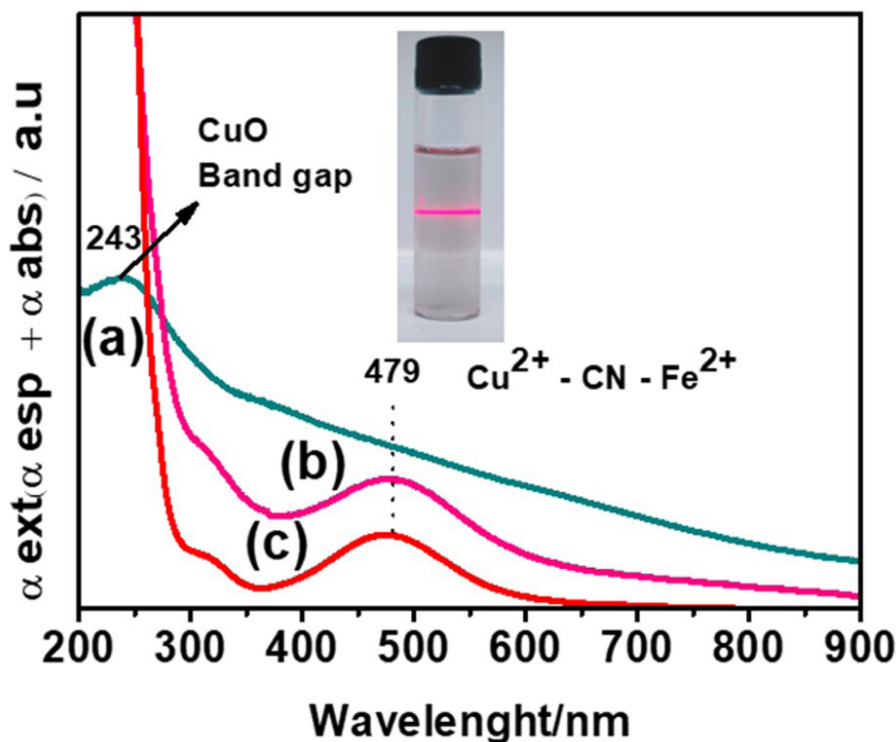

Figure 1. UV-Vis electronic spectra for aqueous dispersions: (a) CuO (0.3 mg mL^{-1}); (b) $Cu_2[Fe(CN)_6]$ (0.1 mg mL^{-1}) and (c) $CuO/Cu_2[Fe(CN)_6]$ (0.1 mg mL^{-1}). Inset: Tyndall effect observed for the nanocomposite.

band gap corresponding to the energy difference between the Cu 3d and O 2p orbitals (Absike et al. 2019). It is interesting to note that the CuO/$Fe_4[Fe(CN)_6]_3$ nanocomposite was the expected product, because ferric and ferrocyanide ions were available in the solution to form PB (with a characteristic absorption band at 690 nm in the UV-Vis spectrum). However, the spectrum in curve c clearly indicates that the formation of CuO/$[Fe(CN)_6]$ occurs without formation of PB.

FTIR spectra (Figure 2) for CuO NPs, $Cu_2[Fe(CN)_6]$, and the nanocomposite in KBr pellets were used to identify the functional groups in the structures, as well as possible interactions. The FTIR spectrum of the $Cu_2[Fe(CN)_6]$ complex shows a strong and broad absorption band between 2600 and 3600 cm^{-1}, which was ascribed to the stretching mode of the O-H group (Gerber & Erasmus 2018). The high-intensity peak at 2103 cm^{-1} observed in the $Cu_2[Fe(CN)_6]$ and CuO/$Cu_2[Fe(CN)_6]$ spectra

was attributed to CN stretching in the Cu(II)–CN–Fe(III) fragment, in agreement with previous work (Gerber & Erasmus 2018). Medium intensity bands at 1605 and 1612 cm^{-1} were assigned to the O-H deformation modes. Additional bands observed at 595 cm^{-1} and 500 cm^{-1} were assigned to Fe-C stretching and Fe-C deformation modes, respectively. The FTIR spectrum for the CuO species (Figure 2a) was found to exhibit three main bands at 1114, 600 and 503 cm^{-1}, which were assigned to δ Cu-O, v_{sym}Cu-O, and v_{asym}Cu-O, respectively, where v and δ denote stretching and angular deformation modes, respectively (Arun et al. 2015, Zhang et al. 2008). The main stretching and deformation bands seen in the FTIR spectra of the PBA and CuO isolated materials were also observed in the FTIR spectrum of the nanocomposite, indicating that the title nanocomposite was formed by addition of $Cu_2[Fe(CN)_6]$ and CuO components. Table I represents our attempt to assign the various
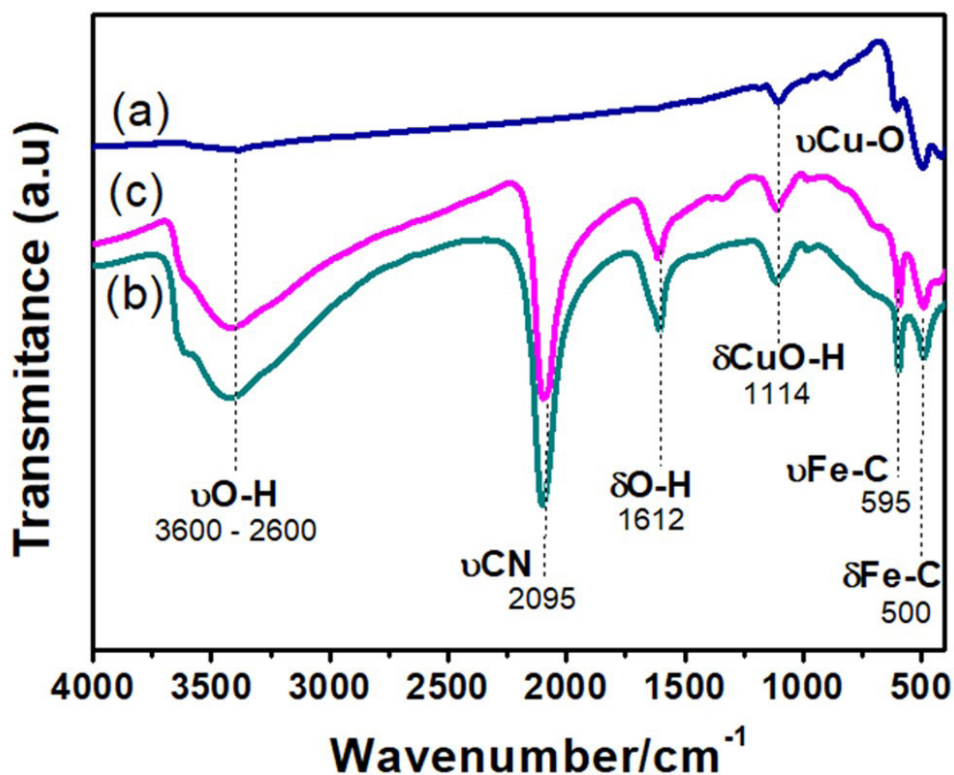

Figure 2. FTIR transmittance spectra in KBr pellets for (a) CuO, (b) the nanocomposite, and (c) the $Cu_2[Fe(CN)_6]$ complex.

bands observed in the FTIR spectra to CuO, $Cu_2[Fe(CN)_6]$, and the nanocomposite.

Crystallinity and morphology study

Figure S4a, b show the diffractograms of the CuO NPs and $Cu_2[Fe(CN)_6]$ with their crystallographic patterns (JCPDS No. 80–1916 and JCPDS No. 03-0513), respectively. Between 10° and 70°, the CuO NPs exhibited eight peaks corresponding to the following crystallographic planes: (110) 32.2°, (002) 34.5°, (11-1) 35.7°, (111) 39.1°, (20-2) 49.5°, (202) 59.3°, (31-1) 62.7° and (200) 67.8°, suggesting the formation of the pure monoclinic phase, as reported by Tamgadge et al. (2019). The $Cu_2[Fe(CN)_6]$ complex exhibited the characteristic peaks of a face-centered cubic (fcc) structure (Jia et al. 2015), corresponding to the following crystallographic planes: (111) 15.4°, (200) 17.8°, (220) 25.2°, (311) 29.8°, (400) 36.2°, (420) 40.6°, (511) 44.5°, (440) 52.3°, (600) 55.7°, and (622) 59.1°. The diffractogram for the nanocomposite shown in Figure S4c clearly indicates the presence of both phases: monoclinic CuO and face-centered cubic $Cu_2[Fe(CN)_6]$, indicating that the nanocomposite has the same phases

as its components. Peaks originating from the $Cu_2[Fe(CN)_6]$ complex are observed at angles corresponding to the planes 222 (17.9°), 220 (25.2°), 440 (35.8°), 420 (40.9°), 400 (50.9°), 600 (59.5°), 600 (62.6), and 620 (68.1°), while the peaks corresponding to the crystallographic planes 111 (39.1°), -202 (49.2°) were attributed to the monoclinic CuO phase. As a result of the ordering and interactions in the nanocomposite, some of the peaks were displaced relative to their positions in the diffraction diagrams of the precursors.

A reduction in crystallinity in the composite was observed from the widening of the highest intensity peak, as estimated by calculating the ratio of width to half peak height of the peak at 39.1° for CuO NPs and for the nanocomposite, indicating a reduction of 55% in the signal corresponding to the crystallographic plane (111) for the CuO component in the nanocomposite. In addition, a decrease in the composite crystallinity was observed using the peak intensity of the crystallographic plane (220) at 17.9 ° for $Cu_2[Fe(CN)_6]$, with a relative reduction of 90% for this signal. Additionally, the broadening

Table I. Assignment of FTIR spectra bands to the CuO, $Cu_2[Fe(CN)_6]$ and nanocomposite.

Material	wavenumber (cm^{-1})
CuO	δ(Cu-O) = 1114; δ_{sym}(Cu-O) = 600; ν ν_{asym}(Cu-O) = 503
$Cu_2[Fe(CN)_6]$	ν(O-H) = 2600 − 3600; ν (C≡N$^-$) = 2103; δ(O-H) = 1612; ν(Fe-C) = 595; δ(Fe-C) = 500
$CuO/Cu_2[Fe(CN)_6]$ Nanocomposite	ν(O-H) = 2600 − 3600; ν(C≡N$^-$) = 2103; δ(O-H) = 1612; ν(Fe-C) = 595; δ(Fe-C) = 500 δ δ(Cu-O) = 1114; δ_{sym}(Cu-O) = 600; ν ν_{asym}(Cu-O) = 503

ν = stretch; δ = angular deformation; sym = symmetric; asym = asymmetric.

of the signals in the composite is attributed to the adsorption and subsequent entrapment of Fe^{3+} ions in the CuO NPs unit cell, as verified by Li et al. (2010). Finally, a high intensity peak was observed at 28.6° in the nanocomposite diffractogram, which can probably be associated with KCl formed during the synthesis. There were no signals corresponding to the iron oxide or hydroxide species.

The size, shape, and organized entities at the molecular level can be analyzed by TEM. The TEM image for CuO NPs (Figure 3a) exhibited rod-like particles of length 20–30 nm, as reported by Nakhaeepour et al. (2019). These small particles form a supramolecular aggregate with a size range of 100 nm to 1 μm, making it difficult to construct a histogram in order to estimate the particle size distribution. The aggregates formed can be attributed to the absence of surfactants that could stabilize the system (Silva et al. 2013) and to nanoparticles associated with a high surface charge (zeta potential ~ 30 mV), as well as to solvent evaporation in the preparation of the sample for TEM analysis (Lopes 2018). Figure 3b shows that the $Cu_2[Fe(CN)_6]$ complex exhibited well-defined spherical shapes with a polydisperse distribution, as observed by Kim et al. (2017). A histogram of the distribution of these particle sizes (shown in Figure S5a)

indicated the presence of particles with a mean diameter of ca. 3.8 nm (using data from 100 nanoparticles). These nanoparticles exhibit small sizes because of their high surface charges (zeta potential -29 mV). In the TEM images for the nanocomposite (Figure 3c), both rod-like structures and spherical shapes, corresponding respectively to the CuO and $Cu_2[Fe(CN)_6]$ species, were observed. A histogram (Figure S5b) of the particle size distribution (using data from 100 nanoparticles) indicated a mean diameter of 5.81 nm. The decrease in size observed for the CuO NPs could be due to interaction with Fe^{3+} species during the synthesis of the $Cu_2[Fe(CN)_6]$ complex in the nanocomposite. The reduced size observed for the CuO NPs is in good agreement with the results reported by Bhuvaneshwari et al. (2016) and Nithya et al. (2019), for CuO NPs after interacting with Cr^{3+} and Ni^{2+} ions, respectively. On the other hand, the $Cu_2[Fe(CN)_6]$ nanoparticles obtained in the nanocomposite showed a significant increase in size (from 3.3 nm in the starting material to 5.81 nm in the composite) but maintained the same spherical shape. It has been proposed that the increase in size of these structures could be due to the higher temperature used in nanocomposite synthesis, which favors the
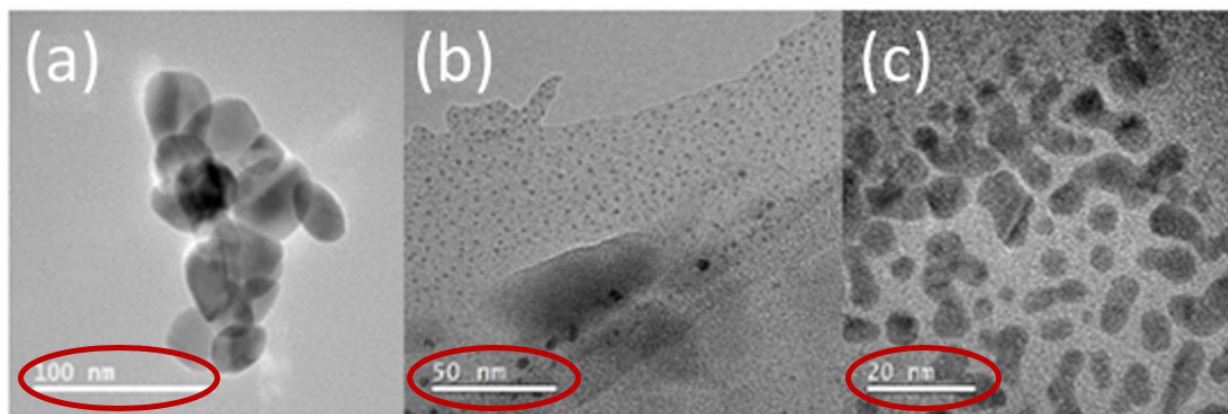

Figure 3. TEM images for (a) CuO NPs, (b) the $Cu_2[Fe(CN)_6]$ complex, and (c) the nanocomposite.

fusion of nanoparticles (Qu et al. 2006, Azam et al. 2012, Xu et al. 2012).

Electrochemical studies of CuO, Cu2[Fe(CN)6], AND CuO/Cu2[Fe(CN)6] modified electrodes

CV was employed to study the electrochemical properties of CuO, $Cu_2[Fe(CN)_6]$, and CuO/$Cu_2[Fe(CN)_6]$ modified electrodes between -0.6 and 1.2 V (*vs* SCE) in a 0.1 mol L^{-1} acetate buffer with a pH of 4.1, using a glassy carbon working electrode. The voltammogram for CuO NPs (Figure 4a) exhibited a quasi-reversible redox pair, with $E_{1/2}$ centered at -0.078 V and a peak-to-peak separation (ΔEp) of 0.123 V at a scan rate of 25 mV s^{-1}, which was assigned to Cu^{2+}/Cu$^+$ conversion (Ba et al. 2016). The electron transfer

at the CuO-modified electrode was evaluated after obtaining voltammograms at different scan rates (10 to 500 mV s^{-1}). It was observed that an increase in the scan rate caused a linear increase in the faradaic currents of the anodic and cathodic peaks, suggesting that electron transfer governs the electrochemical process. The linear correlation between faradaic current and v$^{1/2}$ with correlation coefficient values of 0.9864 and 0.9851 (Figure 4b) demonstrates that the CuO electron transfer is limited by a diffusion process. As illustrated in Figure 4c, $Cu_2[Fe(CN)_6]$ showed a redox-reversible pair with $E_{1/2}$ centered at 0.646 V and a peak-to-peak separation (ΔEp) of 0.143 V at 25 mV s^{-1}, which is characteristic of the CuFe^{2+}/CuFe^{3+} pair (Wang et al. 2011, Zheng
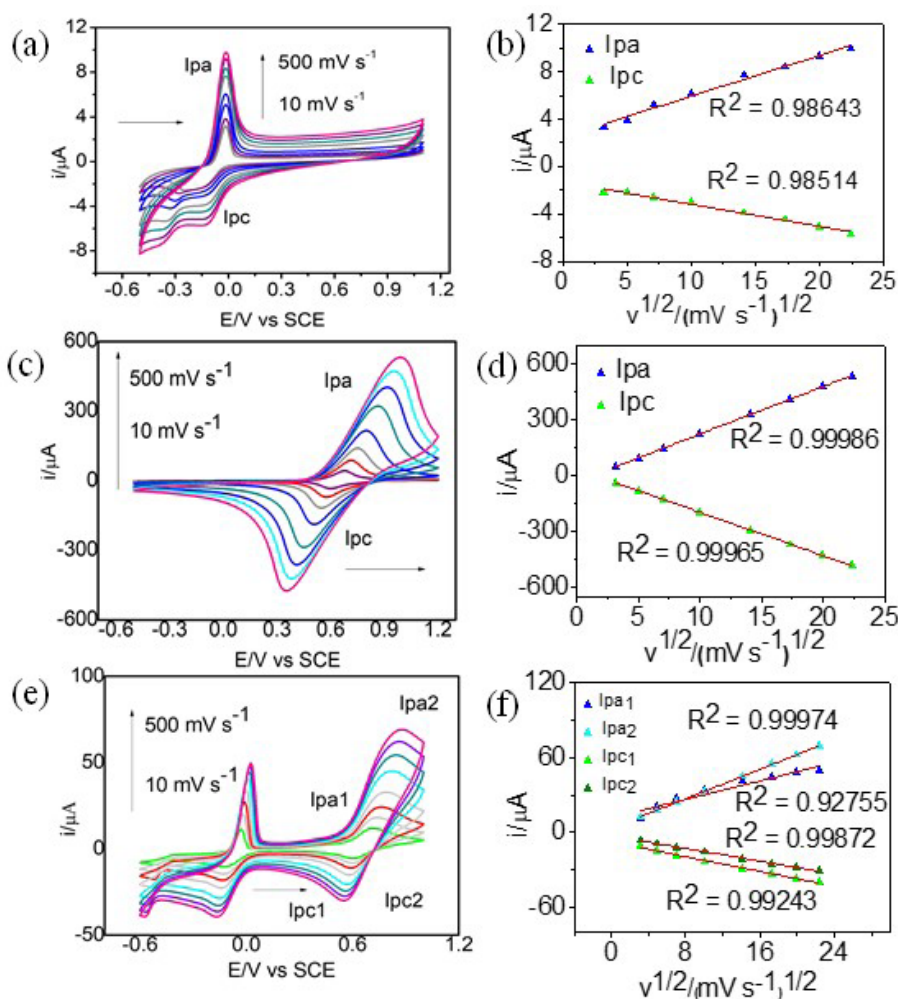

Figure 4. Cyclic voltammograms for glassy carbon electrodes modified with (a) CuO NPs, (c) $Cu_2[Fe(CN)_6]$ complex, and the (e) nanocomposite, with scan rate of 10 to 500 mV s^{-1} in acetate buffer (pH = 4.1) and (b), (d) e (f) study of linearity of currents as a function of v$^{1/2}$.

et al. 2017). The I versus $v^{1/2}$ plot (Figure 4d) was observed to be linear at scan rates up to 500 mV s^{-1}, indicating a diffusion-controlled process. The voltammogram of the CuO/Cu$_2$[Fe(CN)$_6$] nanocomposite (Figure 4e) exhibited two well-defined redox couples at -0.073 (($E_{1/2}$)$_1$) and 0.665 mV (($E_{1/2}$)$_2$), which are attributed to the conversion of Cu^{2+} to Cu$^+$ and CuFe^{2+} to CuFe^{3+} pairs, respectively, which are similar values to those for the CuO and Cu$_2$[Fe(CN)$_6$] precursors. For these electrochemical processes, the peak-to-peak separations were 0.088 and 0.150 V, respectively, at 25 mV s^{-1}. By comparing CuO and Cu$_2$[Fe(CN)$_6$], we observed an increase in the reversibility for Cu^{2+}/Cu$^+$ and CuFe^{2+}/CuFe^{3+} pairs. As observed for the CuO NPs and Cu$_2$[Fe(CN)$_6$] isolated structures, the nanocomposite exhibited a linear profile in the current versus $v^{1/2}$ plot (Figure 4f), indicating a predominantly diffusion-controlled mechanism.

The cyclic voltammograms shown in Figure 5a indicate the well-known electrochemical processes at -0.092 (($E_{1/2}$)$_1$) and 0.644 mV (($E_{1/2}$)$_2$) (ascribed to the Cu^{2+}/Cu$^+$ and CuFe^{2+}/CuFe^{3+} couples, respectively) for the CuO/Cu$_2$[Fe(CN)$_6$]-modified electrode, in the presence of H$_2$O$_2$ at concentrations between 3.0 × 10^{-4} and 3.0 × 10^{-3} mol L^{-1}. The electrode exhibited an electrocatalytic effect toward H$_2$O$_2$, with a linear increase in the faradaic current of reduction after H$_2$O$_2$ addition. In contrast, for the CuO NPs (Figure 5b) and Cu$_2$[Fe(CN)$_6$] (Figure 5c) electrodes, which were used as experimental controls, there was a decrease in the faradaic currents with the addition of peroxide, possibly because there are no interaction sites with H$_2$O$_2$ on the active surface of these electrodes. This is attributed to reactions of the CuO NPs and Cu$_2$[Fe(CN)$_6$] complexes with the peroxide, which would lead to a decrease in the number of electroactive species. Adverse effects are observed in the redox (Cu^{2+}/Cu$^+$) processes of CuO NP structures. Studies by Kamyabi et al. (2017) indicated that the oxidation process is favored with increasing H$_2$O$_2$ concentration, while Gao & Liu (2015b) observed that increased faradaic currents for oxidation and reduction are dependent on peroxide concentration. We observed a substantial increase in reduction processes (Figure 5c), as described by Song et al. (2010). The catalytic effect of peroxide reduction promoted a higher current intensity of the Cu^{2+}/Cu$^+$ pair from the nanocomposite. The significant catalytic effect exhibited by the nanocomposite can be attributed to the decreased crystallinity of this structure, as confirmed by XRD studies
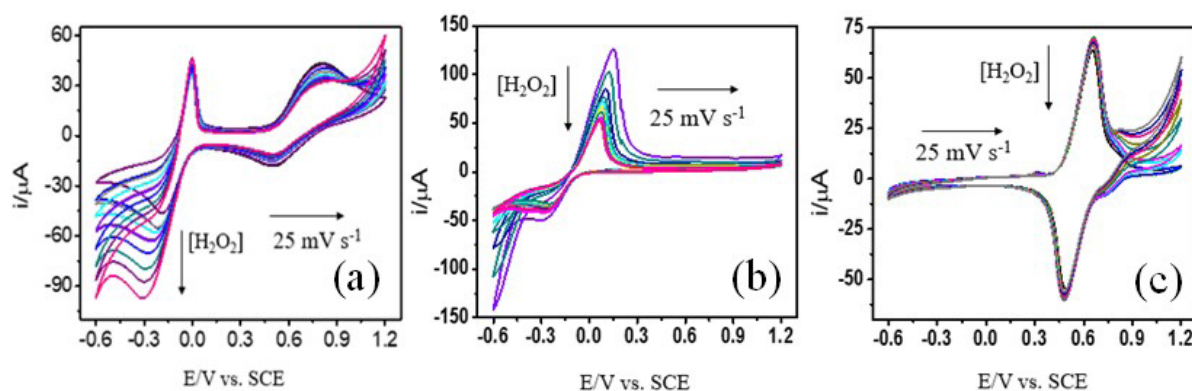

Figure 5. Cyclic voltammograms of the nanocomposite (a), CuO NPs (b) and Cu$_2$[Fe(CN)$_6$] (c) with addition of H$_2$O$_2$ from 3.0 x 10^{-4} to 3.0 x 10^{-3} mol L^{-1} in acetate buffer (pH = 4.1), T = 25 °C, and a scan rate of 25 mV s^{-1}.

(Choudhury et al. 2013). The reduction in crystallinity may be associated with the formation of crystals with structural defects, which favor the formation of a larger number of catalytic sites (Gao et al. 2015a).

CONCLUSIONS

In the present study, we propose a mechanism for the formation of the $CuO/Cu_2[Fe(CN)_6]$ nanocomposite based on the adsorption of Fe^{3+} ions in the CuO structure, with subsequent release of Cu^{2+} ions, as observed by EDS, UV-Vis spectra, and zeta potential analysis. Different synthetic routes using the Fe^{3+} and $[Fe(CN)_6]^{2-}$ precursors led to the formation of PB, but under the reported experimental conditions, the formation of the $CuO/Cu_2[Fe(CN)_6]$ nanocomposite was favored, probably due to the high affinity of the Cu^{2+} species for the cyanide ligand. The nanocomposite showed two well-defined Cu^+/Cu^{2+} and $CuFe^{2+}$ to $CuFe^{3+}$ redox couples in the CV. Additionally, a catalytic effect toward H_2O_2 reduction was observed with increased peak currents for the Cu^+/Cu^{2+} redox process, in contrast to the CuO and $Cu_2[Fe(CN)_6]$ precursors, in which only a slightly enhanced effect for oxidation was observed.

Acknowledgments

REFERENCES

ABSIKE H, HAJJI M, LABRIM H, ABBASSI A & EZ-ZAHRAOUY H. 2019. Electronic, electrical and optical properties of Ag doped CuO through modified Becke-Johnson exchange potential. Superlattices Microstruct 127: 128-138.

AI S, GUO X, ZHAO L, YANG D & DING H. 2019. Zeolitic imidazolate framework-supported Prussian blue analogues as an efficient Fenton-like catalyst for activation of peroxymonosulfate. Colloids Surf A 581: 1-8.

ALFAIFY S & SHKIR M. 2019. A facile one pot synthesis of novel pure and Cd doped PbI_2 nanostructures for electro-optic and radiation detection applications. Opt Mater 88: 417-223.

ALIMARD P. 2019. Fabrication and kinetic study of Nd-Ce doped Fe_3O_4-chitosannanocomposite as catalyst in Fenton dye degradation. Polyhedron 171: 98-107.

ARUN KJ, BATRA AK, KRISHNA A, BHAT K, AGGARWAL MD & FRANCIS PJJ. 2015. Surfactant free hydrothermal synthesis of copper oxide nanoparticles. Am J Mater Sci 5(3a): 36-38.

ASAI M, TAKAHASHI A, TAJIMA K, TANAKA H, ISHIZAKI M, KURIHARA M & KAWAMOTO T. 2018. Effects of the variation of metal substitution and electrolyte on the electrochemical reaction of metal hexacyanoferrate. RSC Adv 8(65): 37356-37364.

AYUBI M, KARIMI M, ABDPOUR S, ROSTAMIZADEH K, PARSA M, ZAMANI M & SAEDI A. 2019. Magnetic nanoparticles decorated with PEGylated curcumin as dual targeted drug delivery: synthesis, toxicity and biocompatibility study. Mater Sci Eng C 104: 1-8.

AZAM A, AHMED AS, OVES M, KHAN MS & MEMIC A. 2012. Size-dependent antimicrobial properties of CuO nanoparticles against gram-positive and negative bacterial strains. Int J Nanomed 7: 3527-3535.

BA N, ZHU L, ZHANG G, LI J & LI H. 2016. Facile synthesis of 3D CuO nanowire bundle and its excellent gas sensing and electrochemical sensing properties. Sens Actuators B 227: 142-148.

BACH LG, THI MLN, SON NT, BUI QB, NHAC-VU HT & AI-LE PH. 2019. Mesoporous gold nanoparticles supported cobalt nanorods as a free-standing electrochemical sensor for sensitive hydrogen peroxide detection. J Electroanal Chem 848: 113359.

BAIONI AP, VIDOTTI M, FIORITO PA & CÓRDOBA DE TORRESI SI. 2008. Copper hexacyanoferrate nanoparticles modified electrodes: A versatile tool for biosensors. J Electroanal Chem 622(2): 219-224.

BHUVANESHWARI S & GOPALAKRISHNAN N. 2016. Enhanced ammonia sensing characteristics of Cr doped CuO nanoboats. J Alloys Compd 654: 202-208.

BIE X, KUBOTA K, HOSAKA T, CHIHARA K & KOMABA S. 2018. Synthesis and electrochemical properties of Na-rich Prussian blue analogues containing Mn, Fe, Co, and Fe for Na-ion batteries. J Power Sources 378: 322-330.

BROWN MD, HALL JR & SCHOENFISCH MH. 2018. A direct and sective electrochemical hydrogen sulfide sensor. Anal Chim Acta 1045: 67-76.

CANTANHÊDE W, SILVA ATB, CARVALHO CLC, MACEDO LJA, MOITA NETO JM & RODRIGUES FILHO UP. 2015. New hybrid nanomaterial based on self-assembly of cyclodextrins and cobalt prussian blue analogue nanocubes. Int J Mol Sci 16(7): 14594-14607.

CARVALHO CLC, SILVA ATB, LUZ RAS, CASTRO GMB, LIMA CL, MASTELARO VR, SILVA RR, OLIVEIRA ON & CANTANHÊDE W. 2018. Development of Co$_3$[Co(CN)$_6$]/Fe$_3$O$_4$ bifunctional nanocomposite for clinical sensor applications. Appl Nano Mater 1(8): 4283-4293.

CHOUDHURY B, DEY M & CHOUDHURY A. 2013. Defect generation, d-d transition, and band gap reduction in Cu-doped TiO$_2$ nanoparticles. Int Nano Lett 3(3): 1-8.

CHU Z, LIU Y & JIN W. 2017. Recent progress in Prussian blue films: Methods used to control regular nanostructures for electrochemical biosensing applications. Biosens Bioelectron 96: 17-35.

DADI R, RABAH A, TRAORE M, MIELCAREK C & KANAEV A. 2019. Antibacterial activity of ZnO and CuO nanoparticles against gram positive and gram negative strains. Mater Sci Eng C 104: 1-9.

DING L, YAN J, ZHAO Z & LI D. 2019. Synthesis of NiGa$_2$O$_4$ nanosheets for non-enzymatic glucose electrochemical sensor. Sens Actuators Chem B 296: 1-5.

FATTAHI A, LIANG R, KAUR A, SCHNEIDER O, ARLOS MJ, PENG P, SERVOS M & ZHOU N. 2019. Photocatalytic degradation using TiO$_2$-graphene nanocomposite under UV-LED illumination: Optimization using response surface methodology. J Environ Chem Eng 7(5): 1-9.

FOROUGHI F, RAHSEPAR M, HADIANFARD MJ & KIM H. 2018. Microwave-assisted synthesis of graphene modified CuO nanoparticles for voltammetric enzyme-free sensing of glucose at biological pH values. Microchim Acta 185: 1-9.

FU G, LIU W, LI Y, JIN Y, JIANG L, LIANG X, FENG S & DAI Z. 2014. Magnetic prussian blue nanoparticles for targeted photothermal therapy under magnetic resonance imaging guidance. Bioconjugate Chem 25(9): 1655-1663.

GAO P, GONG Y, MELLOTT NP & LIU D. 2015a. Non-enzymatic amperometric detection of hydrogen peroxide using grass-like copper oxide nanostructures calcined in nitrogen atmosphere. Electrochim Acta 173: 31-39.

GAO P & LIU D. 2015b. Hydrothermal preparation of nest-like CuO nanostructures for non-enzymatic amperometric detection of hydrogen peroxide. RSC Advances 5: 24625-24634.

GAO ZD, HAN YY, LI YC, YANG M & SONG YY. 2014. Photocatalytic synthesis and synergistic effect of Prussian blue-decorated Au nanoparticles/TiO$_2$ nanotube arrays for H$_2$O$_2$ amperometric sensing. Electrochim Acta 125: 530-535.

GERBER SJ & ERASMUS E. 2018. Electronic effects of metal hexacyanoferrates: An XPS and FTIR study. Mater Chem Phys 203: 73-81.

GHORBANI HR, ALIZADEH V, MEHR FP, JAFARPOURGOLROUDBARY H, ERFAN K & YEGANEH SS. 2018. Preparation of polyurethane/CuO coating film and the study of antifungal activity. Prog Org Coat 123: 322-325.

JELINKOVA P ET AL. 2019. Nanoparticle-drug conjugates treating bacterial infections. J Controlled Release 307: 166-185.

JIA Z, WANG B & WANG Y. 2015. Copper hexacyanoferrate with a well-defined open framework as a positive electrode for aqueous zinc ion batteries. Mater Chem Phys 149-150: 601-606.

KAMILA S & VENUGOPAL VR. 2017. Synthesis and structural analysis of different CuO nanoparticles. Int J Appl Eng 14(3): 133-146.

KAMYABI MA & HAJARI N. 2017. Low Potential and non-enzymatic hydrogen peroxide sensor based on copper oxide nanoparticle on activated pencil graphite electrode. J Braz Chem Soc 28(5): 808-818.

KIM YK, KIM Y, KIM S, HARBOTTLE D & LEE JW. 2017. Solvent-assisted synthesis of potassium copper hexacyanoferrate embedded 3D-interconnected porous hydrogel for highly selective and rapid cesium ion removal. J Environ Chem Eng 5(1): 975-986.

KONG Q, CHEN X, YAO J & XUE D. 2005. Preparation of poly(N-vinyl-2-pyrrolidone)-stabilized transition metal (Fe, Co, Ni and Cu) hexacyanoferrate nanoparticles. Nanotechnology 16(1): 164-168.

KUMAR S, OJHA AK, BHOROLUA D, DAS J, KUMAR A & HAZARIKA A. 2019. Facile synthesis of CuO nanowires and Cu$_2$O nanospheres grown on rGO surface and exploiting its photocatalytic, antibacterial and supercapacitive properties. Phys B 558: 74-81.

LI J, JIANG Y, ZHAI Y, LIU H & LI L. 2015. Prussian blue/reduced graphene oxide composite for the amperometric determination of dopamine and hydrogen peroxide. Anal Lett 48(17): 2786-2798.

LI WJ, HAN C, CHENG G, CHOU SL, LIU HK & DOU SX. 2019. Chemical properties, structural properties, and energy storage applications of Prussian Blue Analogues. Small 15(32): 1-21.

LI Y, XU M, PAN L, ZHANG Y, GUO Z & BI C. 2010. Structural and room-temperature ferromagnetic properties of Fe-doped CuO nanocrystals. J Appl Phys 107(11): 1-6.

LOPES LCS, GOMES KN, BEZERRA TT, BRITO LM, CHAVES MH, CARVALHO FAA & CANTANHÊDE W. 2018. Silver and gold nanoparticles from tannic acid: synthesis, characterization and evaluation of antileishmanial and cytotoxic activities. An Acad Bras Cienc 90: 2679-2689.

MAZEIKIENE R, NIAURA G & MALINAUSKAS A. 2018. Raman spectroelectrochemical study of electrode processes at hybrid polyaniline-copper hexacyanoferrate modified electrode. J Electroanal Chem 808: 228-235.

MOULIK SP, DE GC, PANDA AK, BHOWMIK BB & DAS AR. 1999. Dispersed molecular aggregates. 1. synthesis and characterization of nanoparticles of $Cu_2[Fe(CN)_6]$ in H_2O/AOT/n-heptane water-in-oil microemulsion media. Langmuir 15(24): 8361-836.

NAKHAEEPOUR Z, MASHREGHI M, MATIN MM, NAKHAEIPOUR A & HOUSAINDOKHT MR. 2019. Multifunctional CuO nanoparticles with cytotoxic effects on KYSE30 esophageal cancer cells, antimicrobial and heavy metal sensing activities. Life Sci 234: 1-15.

NERUSH AS, SHCHUKINA KM, BALALAEVA IV & ORLOVA AG. 2019. Hydrogen peroxide in the reactions of cancer cells to cisplatin. Biochim Biophys Acta Gen Subj 1863(4): 692-702.

NITHYA S, SHARAN R, ROY M, KIM HH, ISHIHARA T & DUTTA A. 2019. Ni doping in CuO: a highly sensitive electrode for sensing ammonia in ppm level using lanthanum gallate based electrolyte. Mater Res Bull 118: 1-9.

PEARSON RG. 1963. Hard and Soft Acids and Bases. J Am Chem Soc 85(22): 3533-3539.

PSHINKO GN, PUZYRNAYA LN, SHUNKOV VS, KOSORUKOV AA & DEMCHENKO VY. 2018. Removal of radiocesium from aqueous media with zinc–aluminum layered double hydroxide intercalated with copper(II) hexacyanoferrate. Radiochemistry 60: 395-399.

QUIRINO MR, LUCENA GL, MEDEIROS JA, SANTOS IMG & OLIVEIRA MJC. 2018. CuO Rapid Synthesis with different morphologies by the Microwave hydrothermal method. Mat Res 21(6): 1-9.

QU Y, YANG H, YANG N, FAN Y, ZHU H & ZOU G. 2006. The effect of reaction temperature on the particle size, structure and magnetic properties of coprecipitated $CoFe_2O_4$ nanoparticles. Mater Lett 60(29-30): 3548-3552.

RAWTANI D, THARMAVARAM M, PANDEY G & HUSSAIN CM. 2019. Functionalized nanomaterial for forensic sample analysis. TrAC 120: 1-9.

RICCI F & PALLESCHI G. 2005. Sensor and biosensor preparation, optimisation and applications of Prussian Blue modified electrodes. Biosens Bioelectron 21(3): 389-407.

ROY A, JOSHI M, BUTOLA BS & GHOSH S. 2020. Evaluation of biological and cytocompatible properties in nano silver-clay based polyethylene nanocomposites. J Hazard Mater 384: 1-9.

SANTOS AFM, MACÊDO LJA, CHAVES MH, ESPINOZA-CASTANEDA M, MERKOÇI A, LIMA FCA & CANTANHÊDE W. 2016. Hybrid self-assembled materials constituted by ferromagnetic nanoparticles and tannic acid: a theoretical and experimental investigation. J Braz Chem Soc 27(4): 727-734.

SANTOS GP, MELO AFAA & CRESPILHO FN. 2014. Magnetically controlled single-nanoparticle detection via particle–electrode collisions. Phys Chem Chem Phys 16: 8012-8018.

SILVA ATB, COELHO AG, LOPES LCS, MARTINS MVA, CRESPILHO FN, MERKOÇI A & SILVA WC. 2013. Nano-assembled supramolecular films from chitosan-stabilized gold nanoparticles and cobalt(II) phthalocyanine. J Braz Chem Soc 24(8): 1237-1245.

SINGH M, DOSANJH HS & SINGH H. 2016. Surface modified spinel cobalt ferrite nanoparticles for cationic dye removal: Kinetics and thermodynamics studies. J Water Process Eng 11: 152-161.

SOLIMAN TS & VSHIVKOV SA. 2019. Effect of Fe nanoparticles on the structure and optical properties of polyvinyl alcohol nanocomposite films. J Non-Cryst Solids 519: 1-6.

SONG MJ, HWANG SW & WHANG D. 2010. Non-enzymatic electrochemical CuO nanoflowers sensor for hydrogen peroxide detection. Talanta 80(5): 1648-1652.

SONG Z, LIU W, WEI X, ZHOU Q, LIU H, ZHANG Z, LIU G & ZHAO Z. 2019. Charge storage mechanism of copper hexacyanoferrate nanocubes for supercapacitors. Chin Chem Lett 30(5): 1353-1460

SREEJU N, RUFUS A & PHILIP D. 2018. Nanostructured copper (II) oxide and its novel reduction to stable copper nanoparticles. J Phys Chem Solids 124: 250-260.

TAMGADGE YS, MULEY GG & GANORKAR RP. 2019. Z-scan studies of Sn doped CuO nano-colloidal suspension. Opt Mater 89: 591-597.

TAO Q, ZHANG X, PRABAHARAN K & DAI Y. 2019. Separation of cesium from wastewater with copper hexacyanoferrate film in an electrochemical system driven by microbial fuel cells. Bioresour Technol 278: 456-459.

TEODORO KBR, MIGLIORINI FL, CHRISTINELLI WA & CORREA DS. 2019. Detection of hydrogen peroxide (H_2O_2) using a colorimetric sensor based on cellulose nanowhiskers and silver nanoparticles. Carbohydr Polym 212: 235-241.

THAKUR N, KUMAR M, ADHIKARY SD, MANDAL D & NAGAIAH TC. 2019. PVIM-Co_5POM/MNC Composite as flexible electrode for ultrasensitive and highly selective non-enzymatic electrochemical detection of cholesterol. Chem Commun 55: 5021-5024.

VASANTHARAJ S, SATHIYAVIMAL S, SARAVANAN M, SENTHILKUMAR P, GNANASEKARAN K, SHANMUGAVEL M, MANIKANDAN E & PUGAZHENDHI A. 2019. Synthesis of ecofriendly copper oxide nanoparticles for fabrication over textile fabrics: characterization of antibacterial activity and dye degradation potential. J Photochem Photobiol B 191: 143-149.

VÁZQUEZ ME, LÓPEZ JR, MEDINA-RODELO D, JIMÉNEZ-EDEZA M, CASTAÑEDA-RUELAS GM, LÓPEZ AM, HERRERA-RAMÍREZ JM & MÉNDEZ PF. 2019. Electrochemical study, structural characterization and antimicrobial activity of Silver and Copper Oxide (CuO) nanoparticles synthesized by a Green Method Using L-ascorbic Acid and Chitosan. Int J Electrochem Sci 14: 6366-6375.

VENTURA M, MULLALIU A, CIURDUC DE, ZAPPOLI S, GIULI G, TONTI D, ENCISO E & GIORGETTI M. 2018. Thin layer films of copper hexacyanoferrate: Structure identification and analytical applications. J Electroanal Chem 827: 10-20.

WANG L, WANG Y & ZHUANG Q. 2019. Simple self-referenced ratiometric electrochemical sensor for dopamine detection using electrochemically pretreated glassy carbon electrode modified by acid-treated multiwalled carbon nanotube. J Electroanal Chem 851: 1-7.

WANG X, ZHANG Y, JIANG S, JI X, LIU Y & BANKS CE. 2011. Cubic copper hexacyanoferrates nanoparticles: facile template-free deposition and electrocatalytic sensing towards hydrazine. Int J Electrochem 395724(5): 1-5.

XU X, XU C, DAI J, HU J, LI F & ZHANG S. 2012. Size dependence of defect-induced room temperature ferromagnetism in undoped ZnO nanoparticles. J Phys Chem 116(15): 8813-8818.

XU Y, CHU Z, SHI L, PENG J & JIN W. 2015. Prussian blue nanocubes decorated three-dimensional silver nanowires network for high-performance electrochemical biosensing. Sens Actuators B Chem 221: 1009-1016.

XU Y, ZHENG S, TANG H, GUO X, XUE H & PANG H. 2017. Prussian blue and its derivatives as electrode materials for electrochemical energy storage. Energy Storage Mater 9: 11-30.

ZAKARIA MB & CHIKYOW T. 2017. Recent advances in Prussian blue and Prussian blue analogues: synthesis and thermal treatments. Coord Chem Rev 352: 328-345.

ZHANG L, LU W, FENG Y, NI J, LU Y & SHANG X. 2008. Facile synthesis of leaf-like $Cu(OH)_2$ and its conversion into CuO with nanopores. Acta Phys Chim Sin 24(12): 2257-2262.

ZHENG Y, QIAO J, YUAN J, SHEN J, WANG AJ & NIU L. 2017. Electrochemical removal of radioactive cesium from nuclear waste using the dendritic copper hexacyanoferrate/carbon nanotube hybrids. Electrochim Acta 257: 172-180.

SUPPLEMENTARY MATERIAL

Table SI, Figure SI, Figure SII, Figure SIII, Figure SIV, Figure SV.

WALLONILSON V. RODRIGUES[1,2]
https://orcid.org/0000-0003-3626-8896

STEFFANE Q. NASCIMENTO[1]
https://orcid.org/0000-0002-5869-010X

WESLEY Y.S. SANTOS[1]
https://orcid.org/0000-0001-9267-9679

SANOELLE F.L. QUINZEIRO[2]
https://orcid.org/0000-0001-5754-8358

ROBERTO A.S. LUZ[1]
https://orcid.org/0000-0003-0045-6959

WELTER C. DA SILVA[1]
https://orcid.org/0000-0003-4673-9604

[1]Universidade Federal do Piauí, Departamento de Química, Campus Universitário Ministro Petrônio, Av. Nossa Senhora de Fátima, Ininga, 64049-550 Teresina, PI, Brazil

[2]Departamento de Ensino, Instituto Federal do Maranhão, MA-349, Km 02, Gleba Buriti do Paraíso, Povoado Lamego, 65609-899 Caxias, MA, Brazil

Correspondence to: **Welter Cantanhêde**
E-mail address: welter@ufpi.edu.br

Author contributions

Wallonilson V. Rodrigues and Wesley Y. Santos Silva contributed to the conception, methodology, data curation and writing - original draft. Steffane Q. Nascimento developed the methodology, in special electrochemical studies. Sanoelle Fernanda L. Quinzeiro cooperated with the methodology specially in the on UV-Vis spectroscopy investigations to the composites obtaining. Roberto Alves S. Luz assisted on the conception, supervision and methodology. Welter Cantanhêde carried out the data curation, writing - original draft, supervision, project administration and funding acquisition.